Optical Spectra and Electronic State Structure of Dy^{3+} in Hexagonal $Na_3[Yb_{1-x}Dy_x(dpa)_3]\cdot NaClO_4\cdot 10H_2O$ Crystals†

Todd A. Hopkins, David H. Metcalf, and F. S. Richardson*

Department of Chemistry, University of Virginia, Charlottesville, Virginia 22901

Received March 31, 1995⊗

Polarized optical absorption and emission measurements are used to locate and assign 91 crystal-field energy levels split out of the $4f^9$ electronic configuration of Dy^{3+} in hexagonal $Na_3[Yb_{1-x}Dy_x(dpa)_3]\cdot NaClO_4\cdot 10H_2O$ (x = 0.05, 0.2, 1; dpa ≡ dipicolinate dianion ≡ 2,6-pyridinedicarboxylate). The absorption measurements span the 300−1800 nm wavelength range, and the emission measurements span the 470−775 nm wavelength range. The combined absorption and emission measurements provide access to the energy-level structures of 35 $4f^9$ $[SL]J$ multiplet manifolds of Dy^{3+}, which include *all* multiplet manifolds with baricenter energies < 33 000 cm^{-1} above ground. The site symmetry of the Dy^{3+} ions in hexagonal $Na_3[Yb_{1-x}Dy_x(dpa)_3]\cdot NaClO_4\cdot 10H_2O$ is D_3, and all crystal-field levels split out of the $4f^9(Dy^{3+})$ electronic configuration are Kramers doublets with either E′ or E″ symmetry in the D_3 double-rotation group. Among the 187 crystal-field levels predicted for the 35 multiplet manifolds examined in this study, 91 are both located *and* assigned (with respect to crystal-field symmetry type, E′ or E″, and principal $[SL]J$ multiplet parentage). The 91 assigned levels are analyzed in terms of a model Hamiltonian that includes consideration of both isotropic and non-isotropic 4f-electron/crystal-field interactions. A parametrized form of this Hamiltonian is used to perform parametric fits of calculated-to-experimental energy-level data, and the results obtained from these fits show an rms deviation of 6.3 cm^{-1} between calculated and observed energies. The interaction parameters evaluated from these energy-level data fits are compared to those for Dy^{3+} in other systems, with particular attention given to $Dy(oda)_3^{3-}$ in $Na_3[Dy(oda)_3]\cdot 2NaClO_4\cdot 6H_2O$ (where oda ≡ oxydiacetate). The crystal-field energy-level structures of $Dy(oda)_3^{3-}$ and $Dy(dpa)_3^{3-}$ show significant differences, and these differences are discussed in terms of the ligand moieties that are present in the respective complexes. Among the more than 150 spectral features observed and assigned in the unpolarized axial absorption spectra of $Na_3[Dy(dpa)_3]\cdot NaClO_4\cdot 10H_2O$, 46 are sufficiently well-resolved to permit quantitative determinations of transition line strengths, and these line strengths are reported and discussed.

Introduction

Coordination complexes formed by the chelation of three dipicolinate (dpa) ligands to a trivalent lanthanide ion (Ln^{3+}) have been studied extensively in solution media, where they have been used as nuclear magnetic resonance shift reagents, as sensitizers in photochemical reactions, and as optical probes in studies of intermolecular chiral recognition processes. The coordination chemistry and stereochemical properties of these complexes are reasonably well-characterized, and the optical and magnetic properties of several $Ln(dpa)_3^{3-}$ complexes have also been studied. However, as yet, there have been no measurements reported that permit a *detailed* characterization of the electronic energy-level structure and optical transition properties of a $Ln(dpa)_3^{3-}$ complex. Some optical absorption and emission measurements have been reported for $Eu(dpa)_3^{3-}$, $Tb(dpa)_3^{3-}$, and $Ho(dpa)_3^{3-}$ complexes in solid-state samples at low temperatures,[1-3] but the data obtained from those measurements are either too limited or not sufficiently well-characterized to support detailed energy-level analyses. This situation may be contrasted to that for the structurally similar $Ln(oda)_3^{3-}$ family of complexes (where oda ≡ oxydiacetate), for which there exist extensive and detailed characterizations and analysis of electronic energy-level structure and optical transitions properties.[4] The $Ln(dpa)_3^{3-}$ complexes have been used much more extensively than their $Ln(oda)_3^{3-}$ counterparts as optical and/or magnetic probes in solution-phase studies, but the details of their electronic state structures and optical properties remain relatively unexplored. In the present paper, we report spectroscopic measurements that permit the first detailed analysis of electronic energy-level structure and crystal-field interactions in a $Ln(dpa)_3^{3-}$ complex. The complex is $Dy(dpa)_3^{3-}$, and it is examined in crystalline compounds of stoichiometric formulas $Na_3[Yb_{1-x}Dy_x(dpa)_3]\cdot NaClO_4\cdot 10H_2O$ (x = 0.05, 0.2, 1).

Albertsson has reported single-crystal X-ray diffraction studies on a series of compounds that contain $Ln(dpa)_3^{3-}$ complexes.[5-8] These studies show that the $Ln(dpa)_3^{3-}$ complexes have tris-terdentate chelate structures in which each dpa ligand is coordinated to the Ln^{3+} ion via two carboxylate oxygen donor atoms and a pyridyl nitrogen atom. The LnO_6N_3 coordination polyhedron has a slightly distorted tricapped trigonal prism structure in which oxygen atoms are located at the apices of the trigonal prism and nitrogen atoms are in the capping positions. Each of the three bicyclic chelate rings in a $Ln(dpa)_3^{3-}$ complex has a 2-fold symmetry axis that coincides

* Author to whom correspondence should be addressed.

† dpa ≡ dipicolinate dianion (2,6-pyridinedicarboxylate).

⊗ Abstract published in *Advance ACS Abstracts,* August 1, 1995.

(1) Bolender, J. P.; Metcalf, D. H.; Richardson, F. S. *J. Alloys Compd.* **1992**, *180*, 177.

(2) (a) Murray, G. M.; Sarrio, R. V.; Peterson, J. R. *Inorg. Chim. Acta* **1990**, *176*, 233. (b) Murray, G. M.; Sarrio, R. V.; Peterson, J. R. *Appl. Spectrosc.* **1990**, *44*, 1647. (c) Stump, N. A.; Pesterfield, L. L.; Schweitzer, G. K.; Peterson, J. R. *J. Alloys Compd.* **1992**, *180*, 141. (d) Stump, N. A.; Pesterfield, L. L.; Schweitzer, G. K.; Peterson, J. R.; Murray, G. M. *Spectrosc. Lett.* **1992**, *25*, 1421.

(3) Mondry, A. *Inorg. Chim. Acta* **1989**, *162*, 131.

(4) Metcalf, D. H.; Hopkins, T. A.; Richardson, F. S. *Inorg. Chem.* **1995**, *34*, 4868.

(5) Albertsson, J. *Acta Chem. Scand.* **1970**, *24*, 1213.

(6) Albertsson, J. *Acta Chem. Scand.* **1972**, *26*, 985.

(7) Albertsson, J. *Acta Chem. Scand.* **1972**, *26*, 1005.

(8) Albertsson, J. *Acta Chem. Scand.* **1972**, *26*, 1023.

0020-1669/95/1334-4879$09.00/0

with a Ln−N coordination axis, and taken together, the chelate rings form a three-bladed propeller-like structure of trigonal dihedral (D_3) symmetry. This structure is chiral, with a handedness that reflects the screw sense (or helicity) of the three-bladed propeller assembly. Complexes in which the propeller assembly has a *left-handed* screw sense (about its 3-fold symmetry axis) are generally labeled as Λ, and those in which the propeller assembly has a *right-handed* screw sense are generally labelled as Δ. In solution, $Ln(dpa)_3^{3-}$ complexes exist as a racemic mixture of rapidly interconverting Λ-$Ln(dpa)_3^{3-}$ and Δ-$Ln(dpa)_3^{3-}$ enantiomers,[9] and they also crystallize as racemates. The latter properties preclude the use of chiroptical techniques in spectroscopic investigations of energy-level structure in $Ln(dpa)_3^{3-}$ complexes.

The stereochemical structures of $Ln(dpa)_3^{3-}$ complexes are very similar to those of $Ln(oda)_3^{3-}$ complexes, but these two families of complexes show significant differences in their respective $4f^N(Ln^{3+})$ electronic state structures and optical properties. The pyridyl moieties in a $Ln(dpa)_3^{3-}$ complex exert a stronger influence on $4f^N(Ln^{3+})$ electronic properties than do the corresponding $-CH_2OCH_2-$ ether moieties in a $Ln(oda)_3^{3-}$ complex, and this is reflected in both the crystal-field energy-level structures and 4f → 4f transition intensities observed for $Ln(dpa)_3^{3-}$ *vs* $Ln(oda)_3^{3-}$ complexes. These differences between the electronic properties of $Ln(dpa)_3^{3-}$ and $Ln(oda)_3^{3-}$ complexes have been recognized for some time, on a qualitative level, and they have been addressed in a number of theoretical studies devoted to modelling crystal-field interaction energies and 4f → 4f transition intensities in structurally complex lanthanide systems.[10-12] However, most comparisons between the electronic properties of $Ln(dpa)_3^{3-}$ and $Ln(oda)_3^{3-}$ complexes have, in the past, been based on spectroscopic data acquired from solution-phase measurements, and these data are inadequate for supporting detailed, quantitative analyses of electronic state structure and optical transition properties. The results reported in the present paper for $Dy(dpa)_3^{3-}$, combined with those reported in ref 4 for $Dy(oda)_3^{3-}$, provide the first opportunity for making a detailed comparison of energy levels, optical properties, and crystal-field interactions in a $Ln(dpa)_3^{3-}$ *vs* $Ln(oda)_3^{3-}$ complex.

In the present study, we report optical absorption and emission measurements on single-crystal samples of *hexagonal* $Na_3[Yb_{1-x}Dy_x(dpa)_3]\cdot NaClO_4\cdot 10H_2O$ (x = 0.05, 0.2, 1). The absorption measurements span the 300−1800 nm wavelength range, and they encompass all optical transitions that may occur between the $^6H_{15/2}$ *ground* multiplet and 33 different *excited* multiplet manifolds of the $4f^9(Dy^{3+})$ electronic configuration. The emission measurements span the 470−775 nm wavelength range and encompass all transitions that originate from within the $^4F(3)_{9/2}$ excited multiplet manifold (centered at ca. 21 100 cm^{-1} above ground) and terminate on levels split out of the ^6H_J (J = $^{15}/_2$, $^{13}/_2$, $^{11}/_2$, $^9/_2$) and $^6F_{11/2}$ multiplet manifolds of $4f^9(Dy^{3+})$. The combined absorption and emission measurements provide access to the energy-level structures of 35 $4f^9$ [*SL*]*J* multiplet manifolds of Dy^{3+} (*all* multiplet manifolds with baricenter energies < 33 000 cm^{-1} above ground). These 35 multiplet manifolds include a total of 187 crystal-field levels, each of which is a Kramers doublet with either E′ or E″ symmetry in the D_3 double-rotation group (where E′ corresponds to states with $M_J = \pm^1/_2, \pm^5/_2$ (mod 3) angular momentum properties and E″ corresponds to states with $M_J = \pm^3/_2$ (mod 3) angular momentum properties). Among these 187 crystal-field levels, 91 are both located *and* assigned (with respect to symmetry type *and* principal [*SL*]*J* multiplet parentage) from the optical absorption and emission measurements. Symmetry assignments are based on comparisons of results obtained from both unpolarized *axial* and linearly (σ and π) polarized *orthoaxial* absorption and emission measurements. Optical line strengths are determined for 46 of the transitions observed in the unpolarized *axial* absorption spectra.

The spectroscopic measurements reported here for $Dy(dpa)_3^{3-}$ complexes in *hexagonal* $Na_3[Yb_{1-x}Dy_x(dpa)_3]\cdot NaClO_4\cdot 10H_2O$ crystals closely parallel those reported previously for $Dy(oda)_3^{3-}$ complexes in *trigonal* $Na_3[Dy(oda)_3]\cdot 2NaClO_4\cdot 6H_2O$ crystals.[4] However, whereas chiroptical measurement techniques could be used to good advantage in our spectroscopic investigations of $Dy(oda)_3^{3-}$, these techniques could not be used in our spectroscopic investigations of $Dy(dpa)_3^{3-}$. The *trigonal* $Na_3[Dy(oda)_3]\cdot 2NaClO_4\cdot 6H_2O$ crystals grow as enantiomorphs that contain only one of the configurational isomers (enantiomers) of $Dy(oda)_3^{3-}$, either Λ-$Dy(oda)_3^{3-}$ or Δ-$Dy(oda)_3^{3-}$. However, the *hexagonal* $Na_3[Yb_{1-x}Dy_x(dpa)_3]\cdot NaClO_4\cdot 10H_2O$ crystals contain a racemic mixture of Λ-$Dy(dpa)_3^{3-}$ and Δ-$Dy(dpa)_3^{3-}$ structures and exhibit no *natural* chiroptical activity. We also note that whereas our absorption measurements on $Dy(oda)_3^{3-}$ spanned the 230−1800 nm wavelength range, our absorption measurements on $Dy(dpa)_3^{3-}$ span the more limited 300−1800 nm wavelength range. At wavelengths < 300 nm, the absorption spectrum of $Dy(dpa)_3^{3-}$ is dominated by broad and intense ligand absorption bands that overlay and obscure the much less intense 4f → 4f absorption lines.

The crystal-field energy levels located and assigned for $Dy(dpa)_3^{3-}$ are fewer in number (91) and span a smaller energy range (0−31 545 cm^{-1}) than those located and assigned for $Dy(oda)_3^{3-}$ (152 levels spanning the 0−42 876 cm^{-1} energy range).[4] However, the two data sets are sufficiently compatible to support analyses that are based on fully commensurate model Hamiltonians. The model Hamiltonian employed in our analysis of $Dy(dpa)_3^{3-}$ energy-level data is identical in form to that used for $Dy(oda)_3^{3-}$. This Hamiltonian is constructed to have trigonal-dihedral (D_3) symmetry, and the radially-dependent parts of its interaction terms are treated as adjustable parameters in performing calculated-to-experimental energy-level data fits. Analyses of the $Dy(dpa)_3^{3-}$ energy-level data yield crystal-field interaction parameters that are substantially different from those determined for $Dy(oda)_3^{3-}$, indicating that the crystal-field potential at Dy^{3+} is changed significantly by the substitution of pyridyl moieties for $-CH_2OCH_2-$ ether moieties in the ligand environment.

Experimental Methods

Compound and Crystal Sample Preparation. Hexagonal crystals of $Na_3[Dy(dpa)_3]\cdot NaClO_4\cdot 10H_2O$ were grown in H_2O according to the methods of Albertsson.[7] Stoichiometric amounts of $Dy_2(CO_3)_3$, dipicolinic acid, Na_2CO_3, and $NaClO_4$ were dissolved in H_2O, and the resulting solution was brought to a slightly alkaline pH and subsequently filtered. Morphologically well-defined hexagonal crystals developed from the solution at room temperature over a period of weeks. Hexagonal crystals of stoichiometric formulas $Na_3[Yb_{0.95}Dy_{0.05}(dpa)_3]\cdot NaClO_4\cdot 10H_2O$ and $Na_3[Yb_{0.8}Dy_{0.2}(dpa)_3]\cdot NaClO_4\cdot 10H_2O$ were grown in a similar fashion. Stoichiometric amounts of $Dy_2(CO_3)_3$, $Yb_2(CO_3)_3$, dipicolinic acid, Na_2CO_3, and $NaClO_4$ were dissolved in H_2O; the solutions were brought to a slightly alkaline pH and filtered.

(9) Metcalf, D. H.; Snyder, S. W.; Demas, J. N.; Richardson, F. S. *J. Am. Chem. Soc.* **1990**, *112*, 469.
(10) Stephens, E. M.; Reid, M. F.; Richardson, F. S. *Inorg. Chem.* **1984**, *23*, 4611.
(11) Devlin, M. T.; Stephens, E. M.; Reid, M. F.; Richardson, F. S. *Inorg. Chem.* **1987**, *26*, 1208.
(12) Devlin, M. T.; Stephens, E. M.; Richardson, F. S. *Inorg. Chem.* **1988**, *27*, 1517.

The yield of optical-quality crystals was reasonably good. Crystals harvested were typically well-formed hexagonal plates of *ca.* 1 mm thickness.

Crystals were prepared for spectroscopic measurements by placing them on special copper mounts built for use in the cold head of an optical cryostat (a closed-cycle helium refrigerator). To ensure proper thermal contact, the crystals were wrapped in indium foil at cold head–crystal interfaces. The crystals were mounted in orientations defined with respect to the alignment of their unique (optic) axis relative to the direction of light propagation (in absorption and emission measurements). Parallel alignment of the unique axis and the direction of light propagation is referred to here as an *axial* orientation. Perpendicular alignment of the unique axis and the direction of light propagation is referred to as an *orthoaxial* orientation.

Optical Absorption Measurements. All absorption spectra were obtained with a Cary Model 2415 UV–vis–near-IR spectrophotometer. A CTI-Cryogenic closed-cycle helium refrigerator/cryostat, controlled by a Lake-Shore cryotronics temperature-controller (Model DRC-70), was used to achieve cold-head temperatures of 50 and 10 K. Absorption spectra were recorded over the 300–1800 nm wavelength range. Axial spectra were measured using $Na_3[Dy(dpa)_3]\cdot NaClO_4\cdot 10H_2O$ (DyDPA) crystals, and σ- and π-polarized orthoaxial spectra were measured using $Na_3[Yb_{0.8}Dy_{0.2}(dpa)_3]\cdot NaClO_4\cdot 10H_2O$ (YbDyDPA) crystals. These latter measurements were taken by fitting a linear polarizing element into the spectrophotometer.

Optical line strengths were determined for 46 of the transitions observed in the axial absorption spectra. These line strengths were determined by integrating observed absorbances over transition line profiles and then evaluating

$$S_{i\rightarrow f}(\alpha) = \frac{3.06 \times 10^{-3} g_i}{X_i(T)\,\chi_\lambda c_m b}\int_{i\rightarrow f}\frac{A(\bar{\nu})\,d\bar{\nu}}{\bar{\nu}} \quad (D^2) \qquad (1)$$

where $S_{i\rightarrow f}(\alpha)$ denotes the unpolarized axial line strength of a transition i→f, expressed in units of D^2 (D ≡ 1 debye unit = 10^{-18} esu cm = 3.3356×10^{-30} C m); g_i is the degeneracy of level i; $X_i(T)$ is the fractional thermal (Boltzmann) population of level i at the sample temperature (T); c_m is the molar concentration of Dy^{3+} ions in DyDPA; b is the sample thickness (in cm); χ_λ is a correction factor for bulk sample refractivity at the transition wavelength λ; $A(\bar{\nu})$ denotes the decadic absorbance of the sample at wavenumber $\bar{\nu}$; and the integration is over the absorbance profile of the i → f transition. The molar concentration of Dy^{3+} ions in DyDPA is 1.924 (c_m = 1.924 mol/L); all crystal-field levels of Dy^{3+} in DyDPA are doubly-degenerate (and, therefore, g_i = 2); and all of our unpolarized axial absorption measurements were performed on crystals of 0.2 cm thickness. With this information, eq 1 may be rewritten as

$$S_{i\rightarrow f}(\alpha) = \frac{0.0159}{X_i(T)\,\chi_\lambda}\int_{i\rightarrow f}\frac{A(\bar{\nu})\,d\bar{\nu}}{\bar{\nu}} \qquad (2)$$

Refractive index dispersion data for $Na_3[Ln(dpa)_3]\cdot NaClO_4\cdot 10H_2O$ systems are not available, so the χ_λ factors in our line-strength expressions could not be evaluated. All of the line-strength data reported in this paper are given in units of 10^{-6} D^2/χ_λ.

The surface temperature of the crystals was maintained at 10 K, but analyses of relative line intensities observed in the absorption spectra indicated that the internal temperature of the crystals was *ca.* 20 K. The latter temperature was used in calculating values for the Boltzmann population factors, $X_A(T)$, that appear in eq 1. Integrated areas of absorption lines were determined using computer software. The integration program uses a fitting routine to fit a combination of Gaussian and Lorentzian line shapes to the experimentally observed spectral lines. The program then uses the fitted combination of Gaussian and Lorentzian line shapes to calculate areas.

Optical Emission Measurements. Optical emission spectra were measured using instrumentation constructed in this laboratory. An argon ion laser was used as an excitation source, sample luminescence was dispersed with a 0.75 m double-grating monochromator, and luminescence intensity was measured using photon-counting techniques. In all experiments, sample excitation was along the same direction as that of emission detection. Two different optical cryostats were used to control sample temperature in the emission experiments. A closed-cycle helium refrigerator was used in experiments carried out at 10 and 50 K, and a continuous-flow liquid-helium cooling system was used in experiments carried out at 5 K. Single crystals of either DyDPA or YbDyDPA were mounted with their unique (optic) axes aligned either parallel or perpendicular to the directions of emission detection.

For the hexagonal DyDPA and YbDyDPA crystals examined in this study, emission measured along the crystallographic c axis (i.e., unique axis) is unpolarized , and no polarizing (or analyzing) optical elements were used in our *axial* emission experiments. However, emission measured along a direction that is *perpendicular* to the crystallographic c axis (as in our orthoaxial spectral measurements) can exhibit at least some degree of linear polarization. In our orthoaxial emission experiments, the sample luminescence was analyzed in terms of intensity components polarized perpendicular (σ) and parallel (π) to the crystal c axis. This was done by using a dynamic photoelastic (polarization) modulator that alternately transmitted σ- and π-polarized luminescence intensities to the emission detection unit of our spectrophotometer. The photoelastic modulator (PEM) was a Hinds International Model PEM-80, operated at a modulation frequency of *ca.* 100 kHz.

All of the luminescence observed in our experiments originates from the $^4F(3)_{9/2}$ multiplet manifold of Dy^{3+} (centered *ca.* 21 100 cm^{-1} above ground). The energy gap between this multiplet and the next lower energy multiplet ($^6F_{1/2}$) is *ca.* 7000 cm^{-1}, which is larger than any lattice phonon or molecular vibrational energies in the DyDPA and YbDyDPA crystals. Therefore, nonradiative decay processes for $^4F(3)_{9/2}$ are relatively slow, and this multiplet exhibits a reasonably strong luminescence. In this study, we measured $^4F(3)_{9/2}$ luminescence spectra throughout the $^4F(3)_{9/2} \rightarrow {}^6H_{15/2}$, $^6H_{13/2}$, $^6H_{11/2}$, $^6H_{9/2}$, and $^6F_{11/2}$ transition regions. In all cases, the luminescence was excited with the 476.5 nm line of an argon ion laser, which corresponds to $^6H_{15/2} \rightarrow {}^4F(3)_{9/2}$ excitation.

Data Analysis

Optical Selection Rules and Line Assignments. The symmetry considerations, selection rules, and types of measurements used for making optical transition assignments in the present study are identical to those used in our spectroscopic investigation of $Dy(oda)_3^{3-}$ in $Na_3[Dy(oda)_3]\cdot 2NaClO_4\cdot 6H_2O$,[4] *except* for the absence of any chiroptical measurements. All crystal-field states split out of the $4f^9(Dy^{3+})$ electronic configuration are assumed to reflect the D_3 point-group symmetry of the $Dy(dpa)_3^{3-}$ complexes in *hexagonal* $Na_3[Yb_{1-x}Dy_x(dpa)_3]\cdot NaClO_4\cdot 10H_2O$ crystals, and therefore, each is assumed to have symmetry properties that correspond to either the E′ or E″ irreducible representation (irrep) of the D_3 double-rotation group (denoted here by $\bar{D}_3$). All transitions between crystal-field levels are classified (by symmetry) as E′ ↔ E′, E′ ↔ E″, or E″ ↔ E″, and differences between the electric- and/or magnetic-dipole selection rules for these respective transition types were exploited in making optical line assignments. The relevant selection rules are discussed and shown explicitly in ref 4.

Energy Level Analysis. The energy-level data obtained in this study were analyzed in terms of a model Hamiltonian that has precisely the same form as that described previously in our work on $Dy(oda)_3^{3-}$ (see eqs 3–5 of ref 4). This Hamiltonian assumes D_3 crystal-field symmetry and it is defined to operate entirely *within* the $4f^9(Dy^{3+})$ electronic configuration. The Hamiltonian includes 26 interaction terms, 20 of which represent spherically symmetric interactions that are largely responsible for the ^{2S+1}L (*term*) and $^{2S+1}L_J$ (*multiplet*) structure of the $4f^9(Dy^{3+})$ electronic configuration. The remaining six terms in the Hamiltonian represent non-spherically symmetric crystal-field interactions that can partially remove the $(2J+1)$-fold degeneracies of J-multiplets (of $J \geq {}^3/_2$) and also mix states of different J-multiplet parentage.

As in our previous work on $Dy(oda)_3^{3-}$, a parametrized form of the model Hamiltonian was used in performing the energy-level calculations reported in the present study. The procedures used in carrying out these calculations are identical to those described in ref 4.

Table 1. Calculated and Experimentally Observed Crystal-Field Energy Levels of Dy^{3+} in Hexagonal $Na_3[Dy(dpa)_3]\cdot NaClO_4\cdot 10H_2O$

level no.	term[a]	$2J$[a]	$\lvert 2M_J\rvert$[a]	Γ[b]	energy/cm^{-1} calc[c]	expt[d]	Δ[e]	level no.	term[a]	$2J$[a]	$\lvert 2M_J\rvert$[a]	Γ[b]	energy/cm^{-1} calc[c]	expt[d]	Δ[e]
1	^{6}H	15	7	E′	5	0	5	60	^{4}I(3)	15	13	E′	21956	21957	−1
2	^{6}H	15	9	E″	13	12	1	61	^{4}I(3)	15	9	E″	22010	22003	7
3	^{6}H	15	1	E′	44	50	−6	62	^{4}I(3)	15	11	E′	22027	22032	−5
4	^{6}H	15	11	E′	215	230	−15	63	^{4}I(3)	15	5	E′	22057	22070	−13
5	^{6}H	15	15	E″	229	240	−11	64	^{4}I(3)	15	1	E′	22137	22132	5
6	^{6}H	15	3	E″	257	250	7	65	^{4}I(3)	15	3	E″	22158	22152	6
7	^{6}H	15	13	E′	261	264	−3	66	^{4}I(3)	15	7	E′	22272	22277	−5
8	^{6}H	15	1	E′	286	284	2	67	^{4}I(3)	15	15	E″	22305	22302	3
9	^{6}H	13	1	E′	3545	3542	3	68	^{4}G(4)	11	5	E′	23354	n.d.	
10	^{6}H	13	9	E″	3559	3558	1	69	^{4}G(4)	11	3	E″	23376	n.d.	
11	^{6}H	13	7	E′	3575	3578	−3	70	^{4}G(4)	11	1	E′	23376	23375	1
12	^{6}H	13	11	E′	3605	3605	0	71	^{4}G(4)	11	11	E′	23421	23411	10
13	^{6}H	13	9	E″	3640	3635	5	72	^{4}G(4)	11	9	E″	23442	23451	−9
14	^{6}H	13	5	E′	3657	3652	5	73	^{4}G(4)	11	7	E′	23469	23476	−7
15	^{6}H	13	13	E′	3716	3707	9								
								74	^{4}M	21	19	E′	24904	24912	−8
16	^{6}H	11	1	E′	5844	5850	−6	75	^{4}M	21	17	E′	24932	n.d.	
17	^{6}H	11	9	E″	5866	5873	−7	76	^{4}M	21	15	E″	24937	24939	−2
18	^{6}H	11	5	E′	5922	5919	3	77	^{4}M	21	5	E′	25015	25009	6
19	^{6}H	11	9	E″	5947	5938	9	78	^{4}M	21	1	E′	25063	25066	−3
20	^{6}H	11	7	E′	5951	5945	6	79	^{4}M	21	3	E″	25064	n.d.	
21	^{6}H	11	7	E′	5972	5962	10	80	^{4}M	21	13	E′	25122	25121	1
								81	^{4}M	21	21	E″	25191	25180	11
22	^{6}H	9	7	E′	7574	n.d.		82	^{4}M	21	11	E′	25228	n.d.	
23	^{6}F	11	9	E″	7600	7599	1	83	^{4}M	21	9	E″	25242	n.d.	
24	^{6}F	11	7	E′	7620	7620	0	84	^{4}M	21	7	E′	25250	n.d.	
25	^{6}F	11	3	E″	7719	7716	3								
26	^{6}F	9	1	E′	7751	7756	−5	85	^{4}I(3)	13	5	E′	25574	n.d.	
27	^{6}F	11	11	E′	7771	7772	−1	86	^{4}I(3)	13	11	E′	25603	25593	10
28	^{6}F	11	1	E′	7832	7832	0	87	^{4}I(3)	13	3	E″	25622	n.d.	
29	^{6}H	9	3	E″	7845	7846	−1	88	^{4}F(3)	7	3	E″	25640	25637	3
30	^{6}F	11	5	E′	7870	7866	4	89	^{4}I(3)	13	1	E′	25642	n.d.	
31	^{6}H	9	9	E″	7944	7948	−4	90	^{4}F(3)	7	5	E′	25675	25665	10
32	^{6}H	9	5	E′	8000	n.d.		91	^{4}F(3)	7	1	E′	25685	n.d.	
								92	^{4}I(3)	13	11	E′	25730	25728	2
33	^{6}F	9	7	E′	8917	8919	−2	93	^{4}K(1)	17	15	E″	25752	n.d.	
34	^{6}F	9	9	E″	8982	8990	−8	94	^{4}K(1)	17	11	E′	25760	25763	−3
35	^{6}F	9	1	E′	9025	9034	−9	95	^{4}K(1)	17	11	E′	25790	25790	0
36	^{6}F	9	5	E′	9080	n.d.		96	^{4}K(1)	17	3	E″	25798	n.d.	
37	^{6}F	9	3	E″	9101	9100	1	97	^{4}K(1)	17	5	E′	25803	n.d.	
								98	^{4}K(1)	17	7	E′	25810	n.d.	
38	^{6}H	7	1	E′	9123	n.d.		99	^{4}K(1)	17	1	E′	25823	n.d.	
39	^{6}H	7	5	E′	9196	n.d.		100	^{4}K(1)	17	3	E″	25826	n.d.	
40	^{6}H	7	3	E″	9335	9336	−1	101	^{4}K(1)	17	7	E′	25857	25855	2
41	^{6}H	7	7	E′	9393	9401	−8	102	^{4}K(1)	17	9	E″	25865	n.d.	
								103	^{4}I(3)	13	7	E′	25880	25877	3
42	^{6}H	5	1	E′	10152	n.d.		104	^{4}K(1)	17	17	E′	25899	25890	9
43	^{6}H	5	3	E″	10233	n.d.									
44	^{6}H	5	5	E′	10314	n.d.		105	^{4}M	19	1	E′	26101	26099	2
								106	^{4}M	19	3	E″	26111	n.d.	
45	^{6}F	7	1	E′	10960	n.d.		107	^{4}M	19	17	E′	26136	n.d.	
46	^{6}F	7	3	E″	10989	n.d.		108	^{4}M	19	5	E′	26225	n.d.	
47	^{6}F	7	5	E′	11023	n.d.		109	^{4}M	19	15	E″	26243	n.d.	
48	^{6}F	7	7	E′	11088	n.d.		110	^{4}M	19	13	E′	26283	n.d.	
								111	^{4}M	19	19	E′	26408	n.d.	
49	^{6}F	5	1	E′	12373	n.d.		112	^{4}M	19	11	E′	26450	n.d.	
50	^{6}F	5	5	E′	12402	12400	2	113	^{4}M	19	9	E″	26467	n.d.	
51	^{6}F	5	3	E″	12418	n.d.		114	^{4}M	19	7	E′	26479	n.d.	
52	^{6}F	3	1	E′	13185	13176	9	115	^{4}P(2)	3	3	E″	27258	n.d.	
53	^{6}F	3	3	E″	13189	n.d.		116	^{6}P	5	1	E′	27266	27267	−1
								117	^{6}P	5	3	E″	27292	n.d.	
54	^{6}F	1	1	E′	13731	n.d.		118	^{4}P(2)	3	1	E′	27300	27299	1
								119	^{6}P	5	5	E′	27327	n.d.	
55	^{4}F(3)	9	7	E′	20948	20941	7								
56	^{4}F(3)	9	9	E″	21018	21019	−1	120	^{4}I(3)	11	9	E″	27835	n.d.	
57	^{4}F(3)	9	1	E′	21090	21093	−3	121	^{4}I(3)	11	5	E′	27840	27843	−3
58	^{4}F(3)	9	5	E′	21189	21191	−2	122	^{4}I(3)	11	1	E′	27851	n.d.	
59	^{4}F(3)	9	3	E″	21252	21258	−6	123	^{4}I(3)	11	3	E″	27904	n.d.	

Table 1 (Continued)

level no.	term[a]	$2J^a$	$\|2M_J\|^a$	Γ^b	energy/cm^{-1} calc[c]	expt[d]	Δ^e	level no.	term[a]	$2J^a$	$\|2M_J\|^a$	Γ^b	energy/cm^{-1} calc[c]	expt[d]	Δ^e
124	^{4}I(3)	11	7	E′	27910	27921	−11	156	^{4}G(4)	9	5	E′	30074	30077	−3
125	^{4}I(3)	11	11	E′	27969	n.d.		157	^{4}G(4)	9	1	E′	30114	30115	−1
								158	^{4}G(4)	9	9	E″	30201	n.d.	
126	^{6}P	7	7	E′	28277	n.d.		159	^{4}G(4)	9	7	E′	30221	n.d.	
127	^{6}P	7	5	E′	28313	28314	−1								
128	^{6}P	7	3	E″	28334	n.d.		160	^{6}P	3	3	E″	30573	n.d.	
129	^{6}P	7	1	E′	28339	n.d.		161	^{6}P	3	1	E′	30596	30597	−1
130	^{4}M	15	13	E′	28382	n.d.		162	^{4}K(1)	15	9	E″	31013	n.d.	
131	^{4}M	15	11	E′	28442	n.d.		163	^{4}K(1)	15	7	E′	31016	n.d.	
132	^{4}M	15	9	E″	28443	n.d.		164	^{4}K(1)	15	11	E′	31042	n.d.	
133	^{4}M	15	5	E′	28522	n.d.		165	^{4}L	19	19	E′	31080	n.d.	
134	^{4}M	15	3	E″	28582	n.d.		166	^{4}L	19	11	E′	31112	n.d.	
135	^{4}M	15	1	E′	28616	n.d.		167	^{4}K(1)	15	15	E″	31127	n.d.	
136	^{4}M	15	7	E′	28698	n.d.		168	^{4}L	19	9	E″	31141	n.d.	
137	^{4}M	15	15	E″	28714	n.d.		169	^{4}L	19	5	E′	31144	n.d.	
								170	^{4}L	19	13	E′	31202	n.d.	
138	^{4}F(3)	5	5	E′	29398	29402	−4	172	^{4}K(1)	15	3	E″	31204	n.d.	
139	^{4}F(3)	5	3	E″	29434	29430	4								
140	^{4}I(3)	9	5	E′	29543	29531	12	173	^{4}L	19	11	E′	31215	n.d.	
141	^{4}F(3)	5	1	E′	29571	29575	−4	174	^{4}L	19	15	E″	31254	n.d.	
142	^{4}I(3)	9	3	E″	29597	n.d.		175	^{4}L	19	13	E′	31267	n.d.	
143	^{4}I(3)	9	7	E′	29674	n.d.		176	^{4}L	19	17	E′	31286	n.d.	
144	^{4}I(3)	9	1	E′	29687	29691	−4	177	^{4}L	19	1	E′	31320	n.d.	
145	^{4}I(3)	9	9	E″	29768	29768		178	^{4}L	19	3	E″	31348	n.d.	
								179	^{4}L	19	1	E′	31368	n.d.	
146	^{4}M	17	13	E′	29865	29853	12								
147	^{4}M	17	15	E″	29866	n.d.		180	^{4}G(4)	7	7	E′	31468	n.d.	
148	^{4}M	17	11	E′	29885	29898	−13	181	^{4}G(4)	7	3	E″	31556	31545	11
149	^{4}M	17	3	E″	29943	29945	−2	182	^{4}G(4)	7	5	E′	31570	n.d.	
150	^{4}M	17	1	E′	29960	n.d.		183	^{4}G(4)	7	1	E′	31653	n.d.	
151	^{4}M	17	1	E′	29975	29973	2								
152	^{4}M	17	9	E″	29984	n.d.		184	^{4}D(2)	5	1	E′	31930	n.d.	
153	^{4}M	17	7	E′	29989	n.d.		185	^{4}D(2)	5	3	E″	31956	n.d.	
154	^{4}M	17	11	E′	29993	29997	−4	186	^{4}D(3)	1	1	E′	31987	n.d.	
155	^{4}G(4)	9	3	E″	30027	30049	−22	187	^{4}D(2)	5	5	E′	32024	n.d.	

[a] Identifies the *principal* $SLJM_J$ components of the eigenvectors. [b] Irreducible representation (irrep) label in the $\bar{D}_3$ double-group. [c] Calculated by using the Hamiltonian parameter values listed in Table 2. [d] Experimentally determined locations of energy levels, with $1/\lambda$(air) to $1/\lambda$(vacuum) corrections included. Uncertainties in the energy-level locations are ca. ±3 cm^{-1} (on average). n.d. ≡ not determined. [e] Difference between calculated and observed energies.

Results and Discussion

Energy Levels. The energy levels located and assigned from our optical absorption and emission measurements are shown in Table 1, along with a listing of all *calculated* energy levels between 0 and 33 000 cm^{-1}. The levels are characterized with respect to their principal ^{2S+1}L term and J-multiplet parentages, their major M_J components, their crystal-field symmetry label (E′ or E″) in the $\bar{D}_3$ double-group, and their observed and/or calculated energies. The calculated levels listed in Table 1 were obtained using the Hamiltonian parameter values shown in Table 2. The latter were derived from parametric fits of calculated-to-observed energy-level data. The number of observed levels included in these data fits was 91, and the number of Hamiltonian parameters allowed to freely vary in performing the final data fits was 16. The M^2 and M^4 parameters and the P^4 and P^6 parameters were constrained according the relationships shown in Table 2. The three-body configuration-interaction parameters T^i (i = 2, 3, 4, 6, 7, 8) were treated as free variables in performing a number of early, exploratory data fits, but in the final data fits these parameters were held fixed at the values shown in Table 2. The empirical data set was too small to permit a meaningful exploration of the T^i parts of the overall Hamiltonian parameter space.

The 91 experimental levels listed in Table 1 only include those crystal-field levels that could be characterized with respect to both location (energy) *and* symmetry (E′ or E″) in our optical absorption and emission experiments. These experiments

Table 2. Energy Parameters for the 4f^9 Electronic Configuration of Dy^{3+} in Hexagonal $Na_3[Dy(dpa)_3]\cdot NaClO_4\cdot 10H_2O$

parameter[a]	value[b]/cm^{-1}	parameter[a]	value[b]/cm^{-1}
E_{av}	55912(8)	M^0	3.54(0.12)
F^2	92547(42)	M^2	$0.56M^0$
F^4	65886(177)	M^4	$0.38M^0$
F^6	45182(85)	P^2	792(32)
ζ_{so}	1917(1)	P^4	$0.75P^2$
α	17.8(0.3)	P^6	$0.50P^2$
β	−632(9)	B_0^2	270(20)
γ	1914(46)	B_0^4	−444(27)
T^2	[333]	B_3^4	−725(23)
T^3	[51]	B_0^6	847(37)
T^4	[93]	B_3^6	550(23)
T^6	[−307]	B_6^6	976(21)
T^7	[376]		
T^8	[346]	N^c	91
		σ^d	6.3

[a] Defined according to eqs 4 and 5 in text. [b] Determined by fitting the experimentally observed energy level data listed in Table 1. Parameter values shown in square brackets were held fixed in performing the data fits. [c] Number of assigned energy levels included in the parametric data fits. [d] Root-mean-square deviation between calculated and observed energies (in cm^{-1}).

Table 3. Comparison of Atomic Hamiltonian Parameters Reported for Dy^{3+} in Several Crystalline Hosts

	values/cm^{-1}				
parameter[a]	DyDPA[b]	DyODA[c]	Dy^{3+}:LaF_3[d]	Dy^{3+}:$LaCl_3$[e]	$Cs_2NaDyCl_6$[f]
F^2	92547	93294	91903	92779	92760
F^4	65888	65933	64372	66042	66346
F^6	45183	45624	49386	45686	46358
ζ_{so}	1917	1919	1913	1918	1904
α	17.8	17.5	18.02	17.46	18.4
β	−631	−621	−633.4	−608	−625
γ	1913	1797	1790	1774	1445
T^2	333	345	329	301	311
T^3	51	52	36	12	116
T^4	93	9	127	14	12
T^6	−307	−397	−314	−299	−474
T^7	376	393	404	386	413
T^8	346	330	315	350	315
M^0	3.54	3.34	3.39	2.50	3.34
P^2	792	687	719	501	579
F^2/F^4	1.405	1.415	1.428	1.405	1.398
F^2/F^6	2.048	2.045	1.861	2.031	2.000
F^4/F^6	1.458	1.445	1.303	1.445	1.431

[a] See eq 4 of ref 4. [b] DyDPA ≡ $Na_3[Dy(dpa)_3]$·$NaClO_4$·$10H_2O$. Results from present work (see Table 2). [c] DyODA ≡ $Na_3[Dy(oda)_3]$·$2NaClO_4$·$6H_2O$, where oda ≡ oxydiacetate. Results from Ref. 4. [d] From ref 13. [e] From ref 14. [f] From ref 15.

Table 4. Comparison of Crystal-Field Parameters Reported for Dy^{3+} in Three Crystal Systems Having Trigonal Site Symmetries

	values/cm^{-1}		
parameter[a]	DyDPA(D_3)[b]	DyODA(D_3)[c]	Dy^{3+}:$LaCl_3$(C_{3h})[d]
B_0^2	270	−81	−280
B_0^4	−444	−852	−397
B_3^4	−725	−663	
B_0^6	847	502	527
B_3^6	550	792	
B_6^6	976	742	−288
S^2	270	81	280
S^4	1117	1267	397
S^6	1797	1615	666

[a] The B_m^k crystal-field parameters are defined according to eq 5 of ref 4. The S^k *crystal-field strength* parameters are defined according to $S^k = (|B_0^k|^2 + 2\sum_{m>0}|B_m^k|^2)^{1/2}$. [b] Present work. DyDPA ≡ $Na_3[Dy(dpa)_3]$·$NaClO_4$·$10H_2O$. [c] From ref 4. DyODA ≡ $Na_3[Dy(oda)_3]$·$2NaClO_4$·$6H_2O$. [d] From ref 14.

included measurements carried out on both DyDPA and YbDyDPA crystals, and no discernible differences were observed between the $4f^9(Dy^{3+})$ energy-level structures in the two crystal types. Our parametric fits of the 91 fully characterized crystal-field levels show an rms deviation of 6.3 cm^{-1} between calculated and observed energies.

In Table 3, we show a comparison of the isotropic ("atomic") Hamiltonian parameters reported for Dy^{3+} in five different crystalline hosts, and in Table 4 we compare the crystal-field interaction parameters determined for Dy^{3+} in three different trigonally symmetric systems. In Table 4 we also show values for the "rotational invariant" quantities

$$S^k = (|B_0^k|^2 + 2\sum_{m>0}|B_m^k|^2)^{1/2} \qquad (3)$$

which provide useful measures of the relative strengths of the short-range ($k = 6$) *vs* midrange ($k = 4$) *vs* longer-range ($k = 2$) crystal-field interactions.[16]

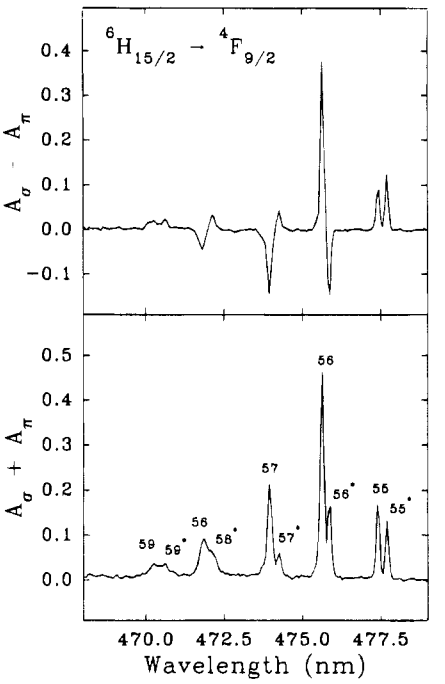

Figure 1. Spectra obtained from linearly polarized, orthoaxial absorption measurements in the $^6H_{15/2} \rightarrow {}^4F(3)_{9/2}$ transition region of Dy^{3+} in hexagonal $Na_3[Yb_{0.8}Dy_{0.2}(dpa)_3]$·$NaClO_4$·$10H_2O$ at 20 K. The crystal thickness was 0.35 cm. Each intensity scale is given in decadic absorbance units. See text for a description of the peak-numbering scheme.

As expected, the atomic Hamiltonian parameters for $Dy(dpa)_3^{3-}$ and $Dy(oda)_3^{3-}$ are quite similar. However, there are some significant differences in the crystal-field interaction parameters determined for $Dy(dpa)_3^{3-}$ *vs* $Dy(oda)_3^{3-}$. First we note that although the S^4 and S^6 crystal-field *strength* parameters show relatively small differences (<15%) between $Dy(dpa)_3^{3-}$ and $Dy(oda)_3^{3-}$, the *anisotropies* within the $k = 4$ and $k = 6$ subsets of B_m^k parameters are quite different for these two systems. Second, we note that the B_0^2 interaction parameters determined for these two systems differ in sign *and* in magnitude, with the B_0^2 parameter for $Dy(dpa)_3^{3-}$ being the larger in magnitude (by a factor of approximately 3.3). The trigonal prismatic DyO_6 structures in $Dy(dpa)_3^{3-}$ and $Dy(oda)_3^{3-}$ are essentially identical, so the observed differences in crystal-field interaction parameters may be attributed entirely to differences between the crystal-field potentials created by the pyridyl *vs* $-CH_2OCH_2-$ (ether) moieties in the respective complexes. Direct calculations of crystal-field interaction strengths in $Ln(dpa)_3^{3-}$ and $Ln(oda)_3^{3-}$ systems suggest that the π-electron distributions on the dpa pyridyl moieties should make especially large contributions to the rank-2 (B_0^2) crystal-field interaction parameter. It is this parameter that provides the largest distinctions between the crystal-field energy-level structures of $Dy(dpa)_3^{3-}$ and $Dy(oda)_3^{3-}$.

Spectra. Examples of the spectra measured and analyzed in the present study are shown in Figures 1−6. The spectra shown in Figures 1−3 were obtained from *linearly polarized, orthoaxial absorption* measurements on a single-crystal sample of $Na_3[Yb_{0.8}Dy_{0.2}(dpa)_3]$·$NaClO_4$·$10H_2O$ at 20 K. In these figures, A_σ and A_π denote decadic absorbances for σ- and π-(linearly-) polarized light. The spectral peak (or line) numbers in these figures identify the *terminal* crystal-field levels involved in individual transitions (see Table 1 for the energy-level

(13) Carnall, W. T.; Goodman, G. L.; Rajnak, K.; Rana, R. S. *J. Chem. Phys.* **1989**, *90*, 3443.
(14) Jayasankar, C. K.; Reid, M. F.; Richardson, F. S. *J. Less-Common Met.* **1989**, *148*, 289.
(15) Tanner, P. A.; Jayasankar, C. K.; Richardson, F. S. *Mol. Phys.* **1988**, *65*, 49.
(16) Leavitt, R. P. *J. Chem. Phys.* **1982**, *77*, 1661.

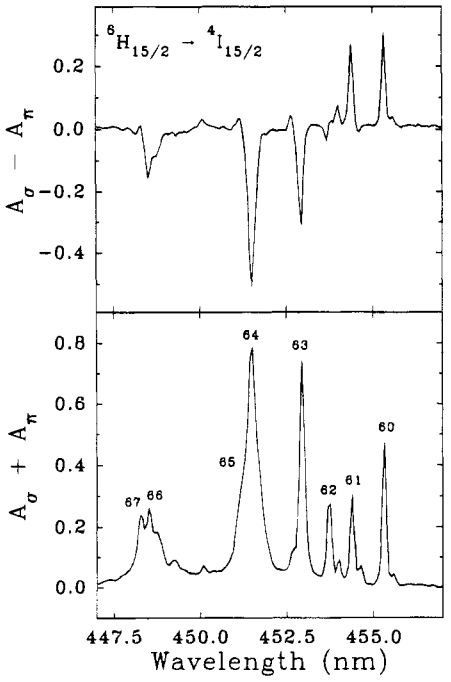

Figure 2. Spectra obtained from linearly polarized, orthoaxial absorption measurements in the $^6H_{15/2} \rightarrow {}^4I(3)_{15/2}$ transition region of Dy^{3+} in hexagonal $Na_3[Yb_{0.8}Dy_{0.2}(dpa)_3]\cdot NaClO_4\cdot 10H_2O$ at 20 K. The crystal thickness was 0.35 cm. Each intensity scale is given in decadic absorbance units. See text for a description of the peak-numbering scheme.

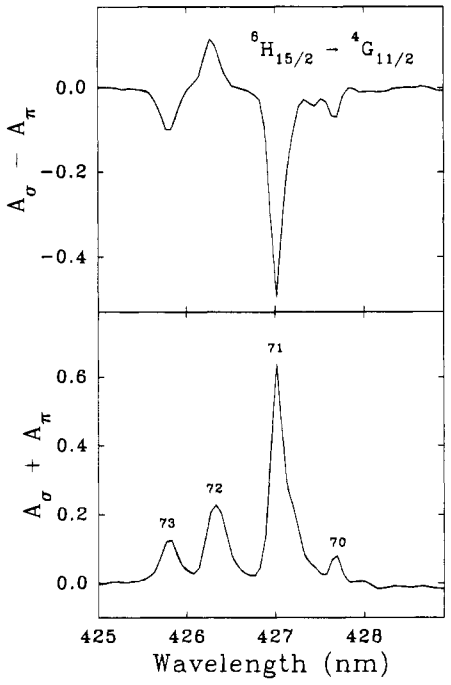

Figure 3. Spectra obtained from linearly polarized, orthoaxial absorption measurements in the $^6H_{15/2} \rightarrow {}^4G_{11/2}$ transition region of Dy^{3+} in hexagonal $Na_3[Yb_{0.8}Dy_{0.2}(dpa)_3]\cdot NaClO_4\cdot 10H_2O$ at 20 K. The crystal thickness was 0.35 cm. Each intensity scale is given in decadic absorbance units. See text for a description of the peak-numbering scheme.

numbering scheme). Peak numbers without asterisks correspond to transitions that originate from the ground crystal-field level of the $^6H_{15/2}$ (ground) multiplet manifold, and peak numbers with an asterisk correspond to transitions that originate from the first excited crystal-field level of $^6H_{15/2}$. The unlabeled features in the spectra correspond to vibronic transitions, an analysis of which lies outside the scope of the present work.

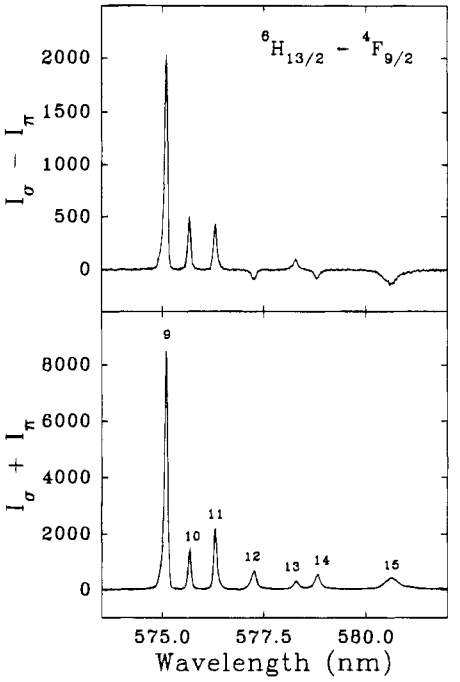

Figure 4. Spectra obtained from linearly polarized, orthoaxial emission measurements in the $^6H_{13/2} \leftarrow {}^4F(3)_{9/2}$ transition region of Dy^{3+} in hexagonal $Na_3[Yb_{0.95}Dy_{0.05}(dpa)_3]\cdot NaClO_4\cdot 10H_2O$ at 5 K. See text for a description of the peak-numbering scheme.

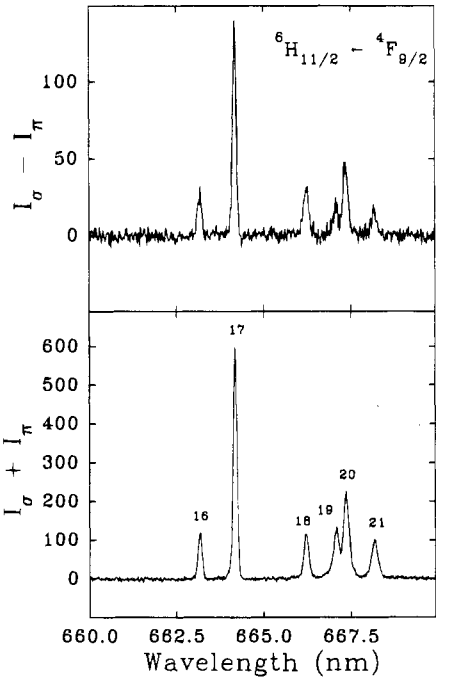

Figure 5. Spectra obtained from linearly polarized, orthoaxial emission measurements in the $^6H_{11/2} \leftarrow {}^4F(3)_{9/2}$ transition region of Dy^{3+} in hexagonal $Na_3[Yb_{0.95}Dy_{0.05}(dpa)_3]\cdot NaClO_4\cdot 10H_2O$ at 5 K. See text for a description of the peak-numbering scheme.

The spectra shown in Figures 4–6 were obtained from *linearly polarized, orthoaxial emission* measurements on a single-crystal sample of $Na_3[Yb_{0.95}Dy_{0.05}(dpa)_3]\cdot NaClO_4\cdot 10H_2O$ at 5 K. In these figures, I_σ and I_π denote σ- and π- (linearly-) polarized emission intensities, expressed in photon counts. All of the emission lines observed in these spectra correspond to transitions that originate from the *lowest* crystal-field level of the $^4F(3)_{9/2}$ multiplet manifold (level 55 in Table 1). The terminal crystal-field levels in these transitions are identified by the spectral peak numbers shown in the figures.

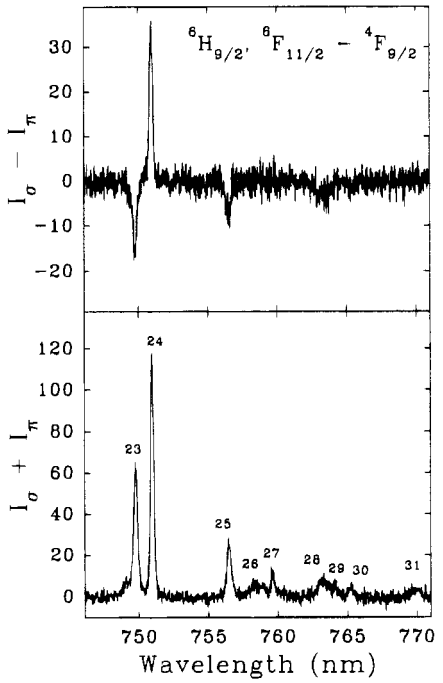

Figure 6. Spectra obtained from linearly polarized, orthoaxial emission measurements in the $^6H_{9/2}$, $^6F_{9/2} \leftarrow {}^4F(3)_{9/2}$ transition region of Dy^{3+} in hexagonal $Na_3[Yb_{0.95}Dy_{0.05}(dpa)_3]\cdot NaClO_4\cdot 10H_2O$ at 5 K. See text for a description of the peak-numbering scheme.

Transition Line Strengths. More than 150 spectral features were observed *and* assigned in the unpolarized axial absorption spectra of $Na_3[Dy(dpa)_3]\cdot NaClO_4\cdot 10H_2O$ (at 20 K). Among these, 46 were sufficiently well-resolved to permit quantitative determinations of transition line strengths. The results obtained from these line-strength determinations are given in Table 5.

The line-strength data given in Table 5 for $Dy(dpa)_3^{3-}$ cover more transition regions than those reported earlier for $Dy(oda)_3^{3-}$, but as was the case for $Dy(oda)_3^{3-}$, the data set is not sufficient to support a definitive parametric analysis based on the Reid–Richardson intensity model for lanthanide 4f → 4f transitions.[17,18] The data could be fitted to the general line-strength expression in this model (see eq 9 of ref 4), but *without* an adequate exploration of the relevant 12-dimensional parameter space. All attempts to fit the empirical line-strength data to a *reduced* (and less general) form of this model, corresponding to the original Judd–Ofelt–Axe theory of 4f → 4f transition intensities,[19–21] were *definitively unsuccessful*. The failure of the less-general intensity model to account for the observed line-strength data has important implications regarding the 4f-electron/ligand-field interaction mechanisms responsible for 4f → 4f electric-dipole intensity. The general intensity model of Reid and Richardson subsumes *all* interaction mechanisms (within the one-electron/one-photon approximation), but the reduced form of this model includes only those interactions that are cylindrically symmetric and pairwise independent.[17,18] In our previous work on $Nd(oda)_3^{3-}$, $Sm(oda)_3^{3-}$, $Eu(oda)_3^{3-}$, and $Ho(oda)_3^{3-}$ systems,[22–27] we showed that the "extra" interaction terms that are included in the general intensity model are *essential* for rationalizing the 4f → 4f transition intensities observed for these systems, and this was attributed to the highly anisotropic (and noncylindrically symmetric) nature of the 4f-electron/ligand-field interactions in these systems. An even

Table 5. Axial Line Strengths Determined for Absorptive Transitions Originating from either the Ground or First Excited Crystal-Field Level of Dy^{3+} in Hexagonal $Na_3[Dy(dpa)_3]\cdot NaClO_4\cdot 10H_2O$

excited level[a]				axial line
no.	multiplet	Γ	$\bar{\nu}^b$/cm^{-1}	strength[c]/10^{-6} D^2
16*	$^6H_{11/2}$	E′	5835	22.3
16	$^6H_{11/2}$	E′	5850	22.2
17	$^6H_{11/2}$	E″	5873	18.8
18*	$^6H_{11/2}$	E′	5907	93.6
18	$^6H_{11/2}$	E′	5919	54.5
25	$^6F_{11/2}$	E″	7716	67.0
33	$^6F_{9/2}$	E′	8919	24.5
34	$^6F_{9/2}$	E″	8990	25.2
35	$^6F_{9/2}$	E′	9034	70.7
40	$^6H_{7/2}$	E″	9336	12.3
41	$^6H_{7/2}$	E′	9401	81.1
50	$^6F_{5/2}$	E″	12400	106.7
52	$^6F_{3/2}$	E′	13176	27.5
55*	$^4F(3)_{9/2}$	E′	20929	4.5
55	$^4F(3)_{9/2}$	E′	20941	2.6
56	$^4F(3)_{9/2}$	E″	21019	7.6
57*	$^4F(3)_{9/2}$	E′	21080	3.5
57	$^4F(3)_{9/2}$	E′	21093	1.4
60*	$^4I(3)_{15/2}$	E′	21945	1.9
60	$^4I(3)_{15/2}$	E′	21957	6.1
61	$^4I(3)_{15/2}$	E″	22003	5.7
62*	$^4I(3)_{15/2}$	E′	22020	4.5
62	$^4I(3)_{15/2}$	E′	22032	3.0
63	$^4I(3)_{15/2}$	E′	22070	7.4
70	$^4G(4)_{11/2}$	E′	23375	0.2
71*	$^4G(4)_{11/2}$	E′	23399	6.0
71	$^4G(4)_{11/2}$	E′	23411	2.5
72	$^4G(4)_{11/2}$	E″	23451	10.4
74*	$^4M_{21/2}$	E′	24898	4.0
74	$^4M_{21/2}$	E′	24912	4.4
76	$^4M_{21/2}$	E″	24939	9.8
77*	$^4M_{21/2}$	E′	24997	2.3
77	$^4M_{21/2}$	E′	25009	3.5
79	$^4M_{21/2}$	E″	25066	17.6
86*	$^4I(3)_{13/2}$	E′	25582	7.0
86	$^4I(3)_{13/2}$	E′	25593	3.8
88	$^4F(3)_{7/2}$	E″	25637	23.6
92	$^4I(3)_{13/2}$	E′	25728	17.2
94	$^4K(1)_{17/2}$	E′	25763	11.9
95	$^4K(1)_{17/2}$	E′	25790	18.7
139	$^4F(3)_{5/2}$	E″	29430	9.6
140	$^4I(3)_{9/2}$	E′	29531	20.6
141	$^4F(3)_{5/2}$	E′	29575	25.4
144	$^4I(3)_{9/2}$	E′	29691	15.1
145	$^4I(3)_{9/2}$	E″	29768	11.7
148	$^4M_{17/2}$	E′	29898	16.0

[a] Terminal level of an absorptive transition, identified according to the level-numbering and -labeling scheme used in Table 1. Asterisks identify transitions that originate from the first excited crystal-field level (no. 2 at 12 cm^{-1} above ground) of the $^6H_{15/2}$ (ground) multiplet. All other transitions originate from the ground-field level of $^6H_{15/2}$. [b] Observed wavenumber (corrected to vacuum) of the absorptive transition. [c] Line strength determined according to eq 1 of the text, without inclusion of the χ_λ correction factor.

(17) Reid, M. F.; Richardson, F. S. *J. Chem. Phys.* **1983**, *79*, 5735.
(18) Reid, M. F.; Richardson, F. S. *J. Phys. Chem.* **1984**, *88*, 3579.
(19) Judd, B. R. *Phys. Rev.* **1962**, *37*, 750.
(20) Ofelt, G. S. *J. Chem. Phys.* **1962**, *37*, 511.
(21) Axe, J. D. *J. Chem. Phys.* **1963**, *39*, 1154.
(22) May, P. S.; Jayasankar, C. K.; Richardson, F. S. *Chem. Phys.* **1989**, *138*, 139.
(23) May, P. S.; Reid, M. F.; Richardson, F. S. *Mol. Phys.* **1987**, *61*, 1471.
(24) May, P. S.; Reid, M. F.; Richardson, F. S. *Mol. Phys.* **1987**, *62*, 341.
(25) Berry, M. T.; Schwieters, C.; Richardson, F. S. *Chem. Phys.* **1988**, *122*, 105.
(26) Moran, D. M.; Richardson, F. S. *Phys. Rev. B* **1990**, *42*, 3331.
(27) Moran, D. M.; Richardson, F. S. *Inorg. Chem.* **1992**, *31*, 813.

greater degree of anisotropy is expected for the 4f-electron/ligand-field interactions in $Ln(dpa)_3^{3-}$ complexes, and, therefore, it is not surprising that the reduced form of the general intensity model fails to account for our $Dy(dpa)_3^{3-}$ line-strength results. However, as was noted above, these results include too few data to support a definitive analysis based on the 12-parameter general intensity model.

All previously reported absorption intensity measurements on $Ln(dpa)_3^{3-}$ systems have focused exclusively on the *total* (integrated) intensities associated with *J*-multiplet-to-*J*-multplet transition manifolds. The line-strength data given in Table 5 are the first to be reported for transitions between individually characterized crystal-field levels.

Conclusion

There is a vast literature on the optical properties and crystal-field energy-level structures of trivalent lanthanide ions in crystalline hosts. Although many different Ln^{3+} coordination environments and site symmetries are represented among the systems examined to date, detailed measurements and analyses of energy-level structure have been confined largely to systems in which the Ln^{3+} ions are coordinated to either monatomic or structurally simple polyatomic ligands (such as, for example, F^-, Cl^-, O^{2-}, or H_2O). The most prominent exceptions to this state of affairs are found in the detailed studies of $Ln(oda)_3^{3-}$ complexes in trigonal $Na_3[Ln(oda)_3]\cdot 2NaClO_4\cdot 6H_2O$ (LnODA) systems. In the LnODA systems, the Ln^{3+} ions are in a structurally complex ligand environment created by terdentate chelation to three oxydiacetate (oda) ligands, and it has been shown that ligand structure beyond the donor-atom coordination core has a strong influence on both the optical properties and the electronic state structure of the Ln^{3+} ions. This is particularly apparent in the strong *chiroptical* properties exhibited by the LnODA systems.

In the present paper, we reported the first detailed analysis of crystal-field energy-level structure in a tris(dipicolinate)-lanthanide(III) complex, $Dy(dpa)_3^{3-}$. The coordination geometry of this complex is very similar to that of $Dy(oda)_3^{3-}$. Both $Dy(dpa)_3^{3-}$ and $Dy(oda)_3^{3-}$ have tris-terdentate chelate structures of trigonal dihedral (D_3) symmetry, and each has a coordination core in which the ligand donor atoms form a slightly distorted tricapped trigonal prism structure. Furthermore, in each case the vertices of the trigonal prism structure are occupied by carboxylate oxygen atoms. However, the two complexes differ with respect to both the chemical and physical nature of the ligand moieties that occupy the equatorial (prism-capping) coordination sites in their respective structures. In $Dy(oda)_3^{3-}$, these sites are occupied by ether oxygen atoms (from $-CH_2-OCH_2-$ groups), whereas in $Dy(dpa)_3^{3-}$ these sites are occupied by pyridyl nitrogen atoms. Although the differences between the *overall* physicochemical structures of $Dy(dpa)_3^{3-}$ and $Dy(oda)_3^{3-}$ are relatively small, they lead to significant differences between the crystal-field energy-level structures of $4f^9$-(Dy^{3+}) in $Dy(dpa)_3^{3-}$ and $Dy(oda)_3^{3-}$. This is apparent from a comparison of the results shown in Table 1 of the present paper and Table 2 of ref 4 and from a comparison of the crystal-field interaction parameters listed in Table 4 of the present paper. The substitution of pyridyl for ether moieties in the three equatorial coordination sites about Dy^{3+} produces significant changes in the 4f-electron/ligand-field interaction strengths *and anisotropies*.

As was noted earlier in the Introduction, $Ln(dpa)_3^{3-}$ complexes have been used extensively as optical and/or magnetic probes in solution-phase studies, and therefore, detailed characterizations of their electronic state structures are of some practical interest and value. The crystal-field analysis performed in the present study for $Dy(dpa)_3^{3-}$, along with the interaction Hamiltonian derived from that analysis, should provide a useful point-of-departure and calibration standard for future work on other $Ln(dpa)_3^{3-}$ complexes. Crystal-field interaction strengths are expected to vary across the lanthanide series, but these variations should show trends that are very similar to those already characterized for the $Ln(oda)_3^{3-}$ series of complexes.[4]

Acknowledgment. This work was supported by the U.S. National Science Foundation (NSF Grant CHE-9213473 to F.S.R.).

IC950365Y